

Controlled probing of Anderson localization and non-Hermitian skin effect via topoelectrical circuits

Dipendu Halder¹ and Saurabh Basu¹

Department of Physics, Indian Institute of Technology Guwahati, Guwahati 781039, Assam, India

(Email of corresponding author: h.dipendu@iitg.ac.in)

The Anderson localization (AL) and the non-Hermitian skin effect (NHSE) are two distinct wavefunction-localization phenomena arising out of disorder and non-reciprocity, respectively. An integration of both in a single framework will provide a platform to study the interplay between the two. In this connection, we consider the one-dimensional Aubry-André (AA) model, which has garnered significant attention among the disordered models due to its self-dual properties. Hence, we investigate a non-reciprocal AA model with complex phase modulation and implement it in suitably designed topoelectrical circuits featuring an interface, segregating two non-equivalent circuit networks. In the circuit, the voltage profile localizes at the interface due to the NHSE, while the AL limits localization phenomena within the vicinity of the excitation node. This competing phenomenon leads to a controllable, node-dependent localization or even partial delocalization of the output voltage. Our results not only provide a practical platform for experimentally studying and controlling the wave localization phenomenon but also highlight the potential of circuit architectures in designing highly sensitive sensors and information transfer in communication devices.

I. INTRODUCTION

Disorders, impurities, and defects are inherent properties of material preparation. A particularly intriguing phenomenon linked to disorder in condensed matter physics is the Anderson localization¹ (AL), which describes how an infinitesimal random disorder induces a transition from an extended to a localized phase in a system in any dimension less than three. Interestingly, AL is not limited to systems with random disorder; quasiperiodic (QP) disorders with incommensurate periods can also result in AL. Among the various QP models, the Aubry-André (AA) model² has garnered significant attention for its theoretical elegance³⁻⁵ and experimental realizations in platforms like photonic crystals⁶⁻⁸, ultra-cold atoms^{9,10}, and superconducting circuits¹¹. A hallmark of the AA model is the absence of mobility edges, that is, an energy-dependent localization transition in the system. This robustness makes the AA model an excellent framework for exploring localization phenomena.

In recent years, non-Hermitian (NH) physics has experienced remarkable growth, finding applications across a wide range of condensed matter systems¹²⁻¹⁵. This exciting area has unveiled a wealth of novel physical phenomena, such as the non-Hermitian skin effect (NHSE)¹⁶⁻¹⁹, where the bulk eigenstates accumulate near the boundaries, and the emergence of exceptional points^{20,21}, where the Hamiltonian becomes defective and eigenvectors coalesce. Additionally, the non-Bloch band theory^{16,22} has redefined the conventional Bloch theorem, offering new insights into the wave behavior for NH systems. Experimental advancements have validated these phenomena in diverse physical platforms, including ultra-cold atoms^{23,24}, mechanical systems²⁵, and acoustic systems²⁶⁻²⁸. These developments have established NH systems as a rich platform for exploring the interplay between topology and non-Hermiticity.

Furthermore, the interplay between disorder and non-hermiticity has also gained significant attention, particularly since the introduction of the Hatano-Nelson (HN) model in

1996²⁹. Through the tight-binding (TB) framework, this one-dimensional (1D) model, characterized by asymmetric hopping and random disorder, reveals the localization transition within the system. Subsequently, NH QP systems have emerged as a vibrant research focus³⁰⁻³⁷. These systems reveal fascinating physics by highlighting the interplay between the NHSE, driven by non-reciprocity, and the AL, induced by quasiperiodicity. Among various experimental platforms, topoelectrical circuits (TECs) have emerged as a powerful tool in modern physics, drawing attention for their ability to map TB Hamiltonians onto circuit Laplacians³⁸⁻⁴³. By adjusting electrical components and connection configurations, TECs offer remarkable flexibility to engineer and explore a wide range of topological states. This unique adaptability enables precise control over coupling coefficients, providing an unprecedented platform for fine-tuning topological phenomena. In TECs, topological edge states are revealed through impedance or voltage profiles, which can be measured by exciting specific nodes within the circuit network. These features make TECs an excellent medium for studying both theoretical and experimental aspects of topology in condensed matter systems. While there have been notable TEC frameworks in realizing both the NHSE⁴⁴⁻⁴⁹ and the AL in QP systems⁵⁰⁻⁵⁴, the intricate interplay between these phenomena remains largely unexplored.

In this work, we examine the competition between the AL and the NHSE, along with their dynamical behavior, by proposing a design of a TEC that serves as a direct classical analog of these quantum localization phenomena. Starting with a 1D NH AA model featuring an interface, separating two non-equivalent AA chains, we notice an emergence of intriguing phenomena arising out of the interplay between AL and NHSE. Utilizing standard circuit elements we construct a TEC capable of replicating both the Hermitian and NH versions of the TB model. By exciting a random node with an external source, we successfully observe the classical analogs of both AL and NHSE. A striking phenomenon emerges when these two compete in a TEC, offering enhanced control over

their dynamics. The novelty of our approach lies in the precise manipulation of the localization of the voltage profile (VP) to specific nodes or ranges within the circuit network, as well as the ability to adjust its amplitude.

The paper is structured as follows: In section II, we introduce the TB model, explaining the underlying physics and the design of the corresponding TEC. The underlying physics of the TB model results is also explored. We also demonstrate the electrical analogs of AL and NHSE in the TEC through voltage measurements via LTspice software. Section III focuses on the interplay between AL and NHSE observed in the TEC. Finally, we summarize our results in section IV and suggest potential experimental setups or devices inspired by the presented theory.

II. THEORETICAL MODEL & TEC

Similar to the Hamiltonian of a TB model, electrical circuit networks operate based on their Laplacians, which govern the network's response at each node⁵⁵. For an electrical network with N_0 nodes, let \mathcal{L} represent the Laplacian, and V_i and I_i denote the voltage and the total current from an external source at the node i . According to Kirchhoff's law, the following

relation holds,

$$I_i = \sum_{k(i \neq k)} X_{ik}(V_i - V_k) + X_i V_i \quad \text{for } k = 1, 2, 3, \dots, N_0, \quad (1)$$

where X_{ik} is the conductance between two distinct nodes i and k . Note that X_{ii} has no physical meaning and is set to zero, while X_i represents the resultant conductance between the node i and the ground. With these definitions, Eq. (1) can be expressed as $I = \mathcal{L}V$, where \mathcal{L} is the $N_0 \times N_0$ Laplacian matrix with elements, $\mathcal{L}_{ik} = -X_{ik} + \delta_{ik}W_i$, where $W_i = \sum_k X_{ik} + X_i$. Thus, the Laplacian \mathcal{L} mirrors a particular second-quantized Hamiltonian of a TB model based on the orientation of the circuit elements.

A. AL & NHSE in a TB model

To design the circuit, we first consider the TB model. Specifically, we adopt the non-reciprocal version of the NH AA model introduced by S. Longhi³⁰, incorporating an interface at a particular lattice site of the chain. The Hamiltonian is given by,

$$H = \sum_{k=1}^{L_0} \left[(t + \gamma) \hat{c}_{k+1}^\dagger \hat{c}_k + (t - \gamma) \hat{c}_k^\dagger \hat{c}_{k+1} \right] + \sum_{k=L_0+1}^{2L} \left[(t - \gamma) \hat{c}_{k+1}^\dagger \hat{c}_k + (t + \gamma) \hat{c}_k^\dagger \hat{c}_{k+1} \right] + \sum_{k=1}^{2L+1} \lambda_k \hat{c}_k^\dagger \hat{c}_k; \quad \lambda_k = 2\lambda \cos(2\pi\beta k + i\alpha), \quad (2)$$

where t , γ , and λ , all possessing positive real values, denote the strengths of the nearest-neighbor hopping, non-reciprocity, and QP disorder, respectively. The system contains $(2L + 1)$ lattice sites, and $(L_0 + 1)^{\text{th}}$ site marks the position of the interface, starting from the first node. The parameter α introduces a complex component to the QP potential. As we will demonstrate, α plays a pivotal role in the TEC, with its prominence becoming evident in the following discussion. β is an irrational number given by $\beta = (\sqrt{5} - 1)/2$ with β^{-1} being the golden ratio. It is obtained via $\beta = \lim_{n \rightarrow \infty} \left(\frac{F_{n-1}}{F_n} \right)$, with the Fibonacci numbers F_n defined recursively by $F_{n+1} = F_n + F_{n-1}$ and $F_0 = F_1 = 1$. The operators \hat{c}_k and \hat{c}_k^\dagger denote the annihilation and creation operators for spinless fermions at the site k . The behavior of the system depends on two scenarios: (a) $\lambda = 0$: in the absence of the QP potential, the system reduces to the clean HN model (no disorder). Here, NHSE arises due to the non-reciprocal hopping parameter γ . (b) $\lambda \neq 0$, $\alpha \neq 0$ but $\gamma = 0$: the model reduces to reciprocal NH AA model that includes the complex QP potential. In the HN model without an interface, all the bulk states accumulate at one of the edges, determined by the sign of the non-reciprocity parameter, γ ¹⁹. The energy spectra for periodic and open boundary conditions are markedly different, with the former creating loops in the complex plane that encloses the latter, which lies along the real axis. For simplicity, we set

$L_0 = L$ in H (Eq. (2)) for further discussions and circuit design. Figure 1(a) depicts the energy spectra of H with $\lambda = 0$. The system exhibits exactly $(L + 1)$ real energy eigenvalues, while the remaining eigenvalues are complex, a stark contrast to the clean HN model without an interface. The probability distribution of the corresponding eigenstates is shown in Fig. 1(b). These eigenstates localize at exactly the middle of the chain, consistent with the sign change in γ at $k = L + 1$ in Eq. (2).

In the presence of the QP potential, the spectrum displays a hierarchical structure of three main bands, which are further split into three sub-bands, as illustrated in Fig. 1(c). In the case of $\gamma = \alpha = 0$, the system undergoes an AL transition at $\lambda = t$, governed by the self-duality of the model. This property ensures that the system is either fully extended or fully localized, dictated solely by the QP potential strength, λ . The introduction of α modifies this behavior, shifting the transition to a critical value of $\ln|V/t|$. This occurs because all the localized eigenstates in the self-dual space share a uniform inverse localization length of $\ln|V/t|$, and when α exceeds this value, the AL transition occurs³⁰. Without α , the localization transition instead occurs at $\lambda = \max(t + \gamma, t - \gamma)$ ⁵⁰, when γ is non-zero. Using Avila's global theory⁵⁶, Li *et al.*³⁷ demonstrated that for a generalized scenario, the AL transition oc-

curs at

$$\alpha_c = \ln |\max(t + \gamma, t - \gamma) / \lambda| \quad (3)$$

Figure 1(d) highlights this scenario through the probability distribution of eigenstates for a high value of α ($\alpha > \alpha_c$), where the AL dominates the NHSE. The dynamical behavior of the TB model, based on different parameters, is explored in Appendix A. Additionally, the study of localization and topological phase transitions in generalized AA models with incommensurately modulated asymmetric hopping offers valuable insights^{34,35}.

B. TEC construction

Now we focus on forming an analog circuit corresponding to the TB model given by Eq. (2). To achieve the goal, the Laplacian of the circuit must accurately replicate the Hamiltonian at the circuit's resonant frequency, f_R . The inter-site hoppings are replaced by capacitors (C), while the non-reciprocity in the hoppings (γ) is introduced via INIC (impedance converter with current inversion) in the circuit. As shown in Fig. 2(a), for the realization of the INIC, an op-amp is employed that works in the negative feedback regime. To ensure circuit stability, two 20Ω resistors are placed parallel to the capacitors⁴⁴. The resonant frequency of the circuit is given by,

$$f_R = \frac{1}{2\pi\sqrt{2LC}} \simeq 5191 \text{ Hz}; \quad \omega_R = \frac{1}{\sqrt{2LC}}, \quad (4)$$

with $L = 10\mu\text{H}$, $C = 47\mu\text{F}$. All these values are kept fixed throughout this work. The real and the imaginary parts of the QP potential, λ_k in Eq. (2), are represented by node-dependent capacitors ($C[k]$) and resistors ($R[k]$), respectively, with $|\text{Re}(\lambda_k)| \equiv \omega_R C[k]$, and $|\text{Im}(\lambda_k)| \equiv R[k]^{-1}$. The value of L' depends on the circuit itself, which shall be discussed later.

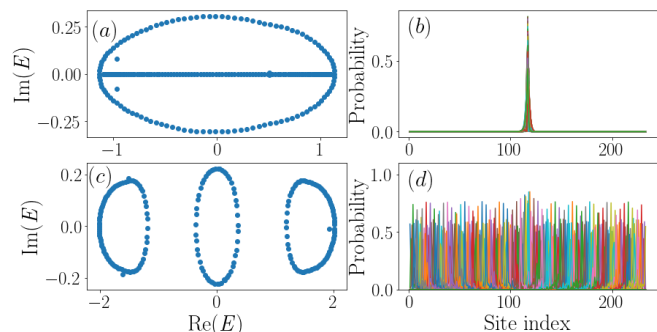


FIG. 1. Numerical analyses for a total number of lattice sites, $(2L + 1) = 233$, being a Fibonacci number, with $t = 0.65$ and $\gamma = 0.35$ are presented. (a) Real vs Imaginary parts of the energy spectra for $\lambda = \alpha = 0$; (b) Probability distribution of the corresponding eigenstates, which localize at site index $(L + 1) = 117$. (c) Same as (a) but with $\lambda = 0.9$, $\alpha = 0.2$. (d) The skin states in (b) have now become AL states as $\alpha > \alpha_c \simeq 0.105$.

All the values of the circuit elements are chosen to be standard commercially available values. The circuit also includes master switches for S and $S1$ (not shown in Fig. 2(b)), which control all S and $S1$ switches across the circuit. For instance, the master switch for S can simultaneously open or close all S switches, and similarly for $S1$. However, this functionality does not extend to $S2$, as $S2$ is specifically designed to alter the signs of $C[k]$ or $R[k]$ based on the values of λ_k , which, in turn, depend on the site index. The total number of nodes is $(2N + 1) = 21$, fixed through the rest of the work. The detailed mathematical rigor behind the Laplacian of this TEC is provided in Appendix B.

To get results in support of the theoretical results in Fig. 1, we will have to obtain the eigenvectors of the Laplacian in terms of measurable quantities like voltage or impedance profile. However, to do that, every node must be excited with a precise source, making the process unnecessarily complicated. Instead, a more practical approach is to excite a single node using a current (or voltage) source and simulate the voltage response of the TEC using the LTspice software, which provides realistic results that align closely with experimental observations. The detailed analysis of this equivalence and the dynamic evolution of the excitation is explained in Appendix C. This method still allows us to observe the localization of the VP, which is equivalent to NHSE and AL in the TB model, as shown in Figs. 1(b) and 1(d), respectively.

C. NHSE in TEC

To realize and explore the NHSE in the non-reciprocal circuit, we open the master switch for S and close the master switch for $S1$ in Fig. 2(b), thereby configuring the TEC to replicate the clean HN model. The grounded inductors at the edges have a distinct value of $L_{\text{edge}} \simeq 62\mu\text{H}$, while the inductor at the $(N + 1)^{\text{th}}$ node, representing the interface, is chosen as $L' \simeq 6\mu\text{H}$. These values differ from the other grounded inductors (L). The role of the non-reciprocity parameter, γ , is implemented using C' ($= 32\mu\text{F}$) along with the INIC. The mapping between the TB model and the circuit is thus established via the relations $(t \pm \gamma) \equiv \omega_R(C \pm C') \simeq (1.53 \pm 1.04)$. Recently, Liu *et al.* demonstrated NHSE at the interface in TECs for both 1D and 2D systems by employing a voltage follower, where the current flows uni-directionally, instead of using an INIC⁴⁵. Both approaches are well-accepted and provide reliable results for constructing non-reciprocal circuits.

To demonstrate a voltage build-up at the interface, we excite the third node with a voltage pulse of amplitude 1 mV for a duration of $10\mu\text{s}$ and record the output signal at each node for 3 ms. To effectively analyze the output, we calculate the root mean square (rms) values of the voltage signal at suitable time intervals for each node. Using LTspice, these data are visualized in a colormap representing the VP as a function of time. The results reveal that the VP localizes at the interface, specifically at node index $(N + 1) = 11$, as shown in Fig. 3. This behavior directly mirrors the NHSE observed in the TB model, as shown in Fig. 1(b). This localization occurs regardless of the node of excitation and the pulse amplitude (or its

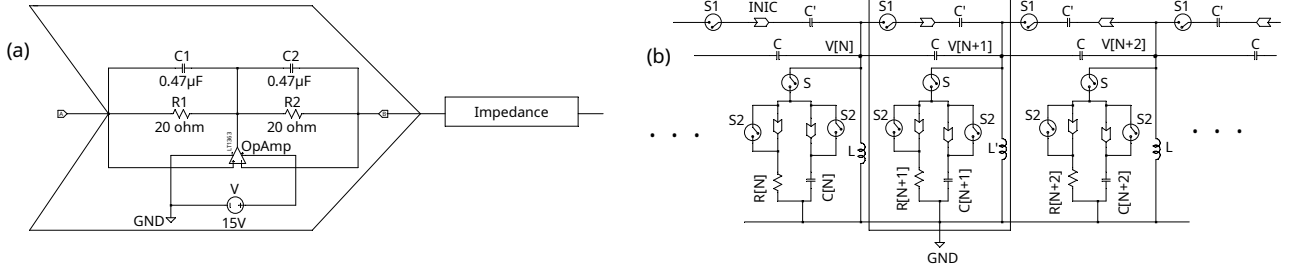


FIG. 2. (a) Circuit diagram of an impedance converter with current inversion (INIC) is shown. The current entering the INIC from the left(right) side experiences a negative(positive) impedance placed in the rectangular box. (b) The TEC diagram corresponds to the non-reciprocal NH AA model. The rectangular box highlights the $(N + 1)^{\text{th}}$ node. $V[N]$ denotes the output voltage at N^{th} node.

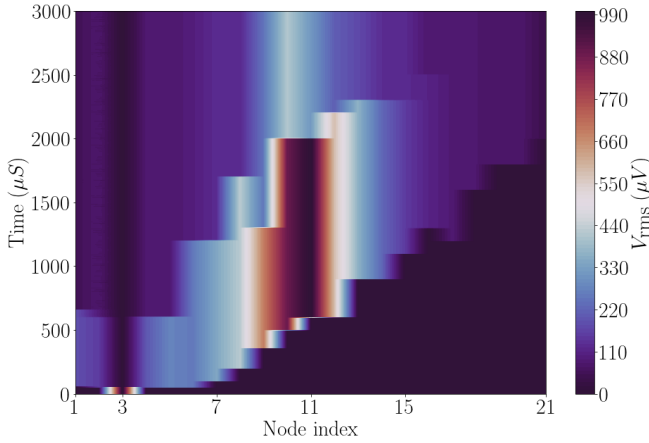


FIG. 3. Colormap of the rms values of the output VP as the functions of both the time and the node index is shown. Commencing around time equal to 0.5 ms and continuing until approximately 2 ms, the VP becomes localized at the interface, whose location is 11^{th} node.

form), demonstrating the robustness of the phenomenon. The voltage amplitude at the interface remains significant for a finite duration post-excitation before gradually decaying due to the short temporal extent of the applied pulse. Interestingly, it parallels the phenomenon of ‘topological funneling of light,’ where a light field within a photonic mesh lattice with an interface is directed toward the interface, irrespective of their shape or the input location⁵⁷. In this case, the excitation is in the form of a voltage pulse, which is directed towards the interface of the circuit.

D. AL in TEC

As depicted in Fig. 2(b), to isolate and observe the AL, we close the master switch for S , while keeping $S1$ open. The only practical method to implement the onsite QP potential in the circuit involves individually placing capacitors and resistors

obeying the following equations, namely,

$$C[k] = -\text{Re}(\lambda_k)/\omega_R = -2\lambda \cos(2\pi\beta k) \cosh \alpha/\omega_R, \quad (5)$$

$$R[k] = [\text{Im}(\lambda_k)]^{-1} = [-2\lambda \sin(2\pi\beta k) \sinh \alpha]^{-1}, \quad (6)$$

derived from the expression of λ_k in Eq. (2). It is crucial to note that both $\text{Re}(\lambda_k)$ and $\text{Im}(\lambda_k)$ being oscillatory functions, can assume negative values, and consequently, $C[k]$ and $R[k]$ may be negative. To avoid negative capacitance values, a constant capacitor can be grounded⁵⁴, ensuring no impact on the central results. However, this strategy is not feasible for resistors ($R[k]$), as additional grounded resistors would unnecessarily increase circuit dissipation. As a remedy, we make the resistors negative using INIC. While INIC primarily ensures non-reciprocal current flow between nodes, when one node is grounded (as is the case in our setup), it does not affect the circuit’s Laplacian and yields desired outcomes. Therefore, the absolute values of $C[k]$ and $R[k]$ are placed at each node based on $|\text{Re}(\lambda_k)|$ and $|\text{Im}(\lambda_k)|$, respectively. $S2$ switches are carefully toggled (closed or opened) at each node depending on the signs of $\text{Re}(\lambda_k)$ and $\text{Im}(\lambda_k)$. Moreover, the grounded inductors at the edges have a value of $L_{\text{edge}} = 20 \mu\text{H}$, while L' is identical to L as there exists no interface in this case.

Fig. 4 illustrates the VP as a function of α , with $\lambda = 1$ in Eq. (2), under the condition where a constant current source of amplitude 1 mA and frequency f_R , as defined in Eq. (4), is applied to the fourth node. For the TB model, the AL transition should occur at the critical value α_c , calculated using Eq. (3), with $\gamma = 0$. The red dashed line in the figure marks this critical value, $\alpha_c \simeq 0.425$. However, due to practical factors such as the finite system size (only 21 nodes) and simulational limitations of LTspice, a sharp transition is not observed. Nevertheless, the results demonstrate that for $\alpha > \alpha_c$, the VP becomes predominantly localized at the fifth node. When the simulation is repeated with excitation at different nodes (not shown here), the localization consistently occurs in the vicinity of the respective excitation node, highlighting a predictable and robust localization center. This predictability sharply contrasts with the phenomenon of NH jumps^{58,59}, where wave packet evolution transpires not through gradual diffusion, but through sudden transitions between distant states. Such NH jumps are highly sensitive to the initial conditions and the intrinsic prop-

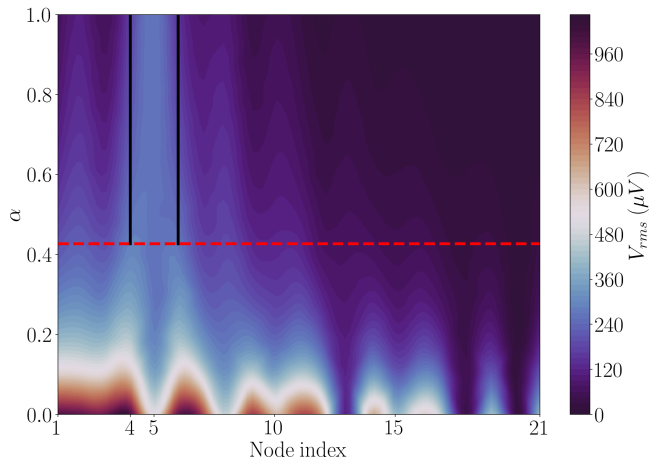


FIG. 4. The rms values of the output signal, measured over the duration from 0.6 ms to 2 ms , are presented as functions of the node indices and α . The red dashed line denotes the critical value of α , namely, α_c , obtained from Eq. (3). The two black vertical lines outline the localization of the VP at the fifth node for $\alpha > \alpha_c$.

erties of the system, unlike the reliable and consistent localization behavior observed in this TEC.

III. COMPETITION BETWEEN AL & NHSE

The interplay between NHSE and AL in the TB model exhibits fascinating behavior in localization transition. AL directs a single-site excitation toward a ‘focal point,’ determined by the weight factors based on the overlap between the initial excitation and exponentially localized eigenstates⁵⁸, while NHSE drives it to an interface (or the edges). To interpret this interplay in the TEC, we close both S and $S1$ to incorporate both the non-reciprocity and the QP potential and again excite the fourth node with a current source, as described earlier. Fig. 5(a) shows that when the QP disorder is real ($\alpha = 0$), the disorder potential is weak compared to the non-reciprocity parameter (γ) to draw the signal toward the excitation node. However, once α surpasses the critical value $\alpha_c \simeq 0.54$ (determined using Eq. (3)), the localization of the output voltage shifts to the excitation (fourth) node. The VP for $\alpha = 1$ closely resembles the situation illustrated in Fig. 1(d). An intriguing aspect of this behavior is that the output amplitude is diminishing with increasing α . This reduction is attributed to the significant rise in $|R[k]|$, which scales with $\sinh^{-1} \alpha$ (Eq. (6)). Consequently, by tuning α , one can effectively control both the spatial localization and the power of the output signal. This dual ability to modulate the NHSE and the AL dynamics is a distinctive feature of our TEC with potential applications similar to information transfer communication devices or the development of highly sensitive sensors.

Upon closer inspection, a gradual increase in α from zero to α_c while keeping λ fixed ($\lambda = 1.5$ in this case) unveils a peculiar phenomenon. In the TEC, as previously discussed, AL is spatially confined over a short range near the excitation node.

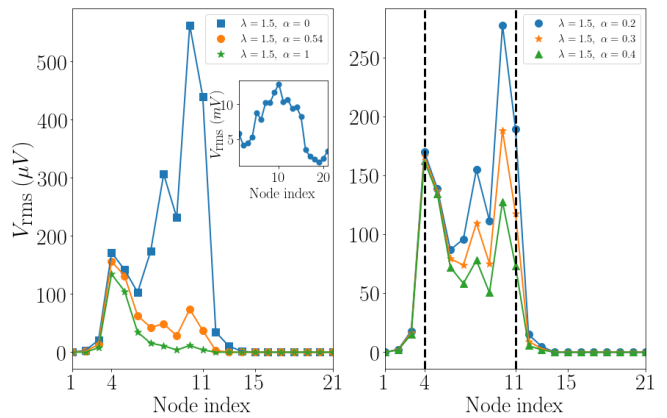


FIG. 5. (a) The rms values of the VP are plotted for different values of α for $\lambda = 1.5$, measured over the duration 1 ms to 3 ms . The VP moves towards the fourth node at $\alpha = \alpha_c$ with a much smaller amplitude. The inset depicts the VP in the absence of any QP potential $\lambda = 0$, measured over the duration 2 ms to 5 ms . Note that all the values are in mV , which suggests voltage amplification, compared to the constant external signal, for a sufficiently longer time. (b) The same profile, but for values of α between zero and the critical value (α_c). The two black-dashed vertical lines enclose the key nodes (exciting and interface nodes), that contain the partial delocalization of the VP.

On the other hand, NHSE drives the excitation towards the interface. This interplay generates a fascinating *tug-of-war* between the NHSE and the AL-induced localization, resulting in a ‘partial’ delocalization of the output signal within a defined spatial range. This range is bounded by two controllable key nodes, namely, the interface and the excitation node. Fig. 5(b) illustrates this phenomenon, where the VP shows non-zero oscillations between the fourth and the eleventh nodes, beyond which VP decays to zero. During the transition, the amplitude of the output signal becomes somewhat uniform across the intermediate nodes, effectively creating a spatial channel for the signal. Furthermore, the position and width of this channel can be tuned by altering the excitation node or the interface of the circuit, offering versatile control over the behavior of the input signal. Thus, as said earlier, α serves as a critical parameter, acting as a switch that toggles between the impact of NHSE and AL on the spreading dynamics of a single-site excitation.

IV. SUMMARY

In this work, we have explored the non-Hermitian skin effect and the Anderson localization in a tight-binding model, where the former occurs due to non-reciprocal hoppings, and the latter is driven by quasiperiodic disorder. To experimentally visualize these quantum phenomena and their interplay, we have proposed a topoelectrical circuit as its classical realization. Our findings demonstrate how the output of an electrical circuit, designed to mimic a theoretical model, can precisely be controlled using principles rooted in the quantum regime. The dynamic behavior of these contrasting quantum phenom-

ena is quite tangible and experimentally accessible in electrical circuits, establishing them as a convenient platform for investigating such interplay. This quantum-to-classical correspondence not only deepens our understanding of the skin effect and the Anderson localization but also opens new avenues for designing advanced sensors or information transfer in electronic devices, leveraging the tunability and versatility of electrical circuits to emulate and harness quantum effects.

V. AUTHOR DECLARATIONS

Conflict of Interest

The author has no conflicts to disclose.

VI. DATA AVAILABILITY STATEMENT

The data that support the findings of this study are available within the article.

APPENDIX A: DYNAMICAL BEHAVIOR OF THE TIGHT-BINDING MODEL

We have explored the localization properties of the eigenstates of the Hamiltonian for the non-Hermitian (NH) Aubry-André (AA) model given by (we reproduce it from the main text for convenience),

$$H = \sum_{k=1}^{L_0} \left[(t + \gamma) \hat{c}_{k+1}^\dagger \hat{c}_k + (t - \gamma) \hat{c}_k^\dagger \hat{c}_{k+1} \right] + \sum_{k=L_0+1}^{2L} \left[(t - \gamma) \hat{c}_{k+1}^\dagger \hat{c}_k + (t + \gamma) \hat{c}_k^\dagger \hat{c}_{k+1} \right] + \sum_{k=1}^{2L+1} \lambda_k \hat{c}_k^\dagger \hat{c}_k, \quad (7)$$

where $\lambda_k = 2\lambda \cos(2\pi\beta k + i\alpha)$. All the parameters have been elaborated upon in the main text. An intriguing question arises:

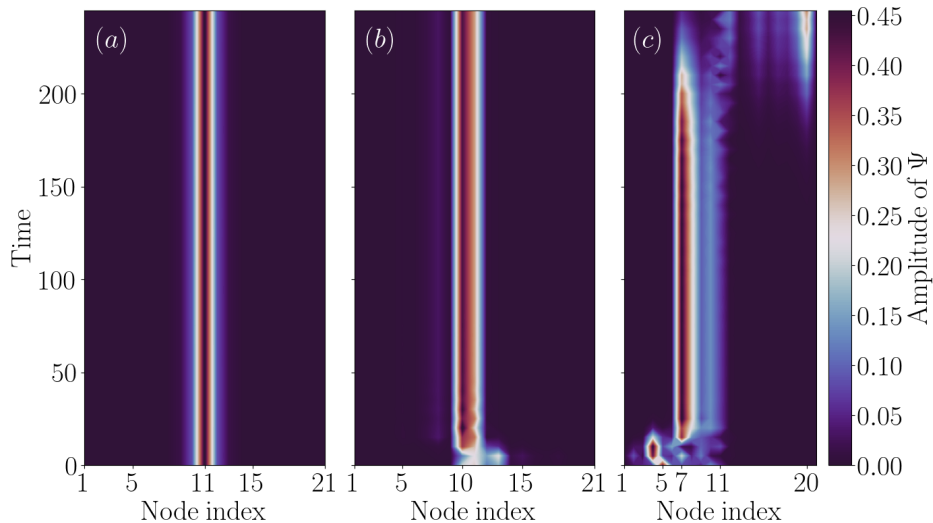


FIG. 6. The temporal evolution of the excitation in the non-reciprocal NH AA model is illustrated for three scenarios: (a) $\lambda = 0$, (b) $\lambda = 1$, $\alpha = 0.425$, and (c) $\lambda = 1$, $\alpha = 0.9$. In the first case, the localization of the wavefunction at the interface is attributed to the NHSE. In the second case, at $\alpha = \alpha_c$, a slight shift in the localization is observed. Finally, for a much larger value of α , the wavefunction undergoes brief transitions, namely, from the 5th site to the 4th site, then to the 7th site for an extended period, and ultimately localizes at the 20th site.

does the interplay between the non-Hermitian skin effect (NHSE) and the Anderson localization (AL) persist over long time scales, or do the dynamics of the system unveil any interesting physics? To address this, we investigate the dynamic evolution of an excited wavefunction at any spatial position in the NH AA model. Let the initial wavefunction at $t = 0$ be $|\Psi(x, 0)\rangle$, which can be expanded as a linear combination of the eigenstates of H in Eq. (7), given as,

$$|\Psi(x, 0)\rangle = \sum_{k=1}^{2L+1} a_k \psi_k, \quad (8)$$

where a_k is the projection coefficient corresponding to the k^{th} eigenstate, ψ_k . As an initial condition, we choose a delta-type excitation of the form, $|\Psi(x, 0)\rangle = \delta(x - m)$, which is localized entirely at the m^{th} site and is zero elsewhere. Note that x is

discrete and lies in the range $x \in [1, 2L + 1]$. The time evolution of $|\Psi(x, 0)\rangle$ governed by the Schrödinger equation, is given by,

$$|\Psi(x, t)\rangle = e^{-iHt} |\Psi(x, 0)\rangle. \quad (9)$$

This equation is specifically applicable to systems without boundaries, where x ranges from $-\infty$ to $+\infty$. However, as long as the wavefunction acquires a nearly zero probability density at the boundaries, that is, eliminating the possibility of reflection of the excited state during its evolution, we can reliably use Eq. (9) to determine $|\Psi(x, t)\rangle$ at all subsequent times.

NH systems are known for their non-conservation of energy, leading to non-unitary dynamics. As a result, these systems violate probability conservation, resulting in the norm of the wavefunction to either grow or diminish over time. Thus, we have to normalize the amplitude of the final wavefunction with its norm every time. The evolution of the wavefunction after a small interval dt occurs through a two-step process⁶⁰. First, the wavefunction evolves as,

$$|\Psi(t + dt)\rangle = e^{-iHdt} |\Psi(t)\rangle. \quad (10)$$

This is hence followed by a normalization step,

$$|\Psi(t + dt)\rangle = \frac{|\Psi(t + dt)\rangle}{\| |\Psi(t + dt)\rangle \|}, \quad (11)$$

where $\| \cdot \|$ denotes the vector norm.

Let us now employ Eqs. (10) and (11) to numerically analyze $|\Psi(x, t)\rangle$. The hopping parameters are set as $(t \pm \gamma) = (1.53 \pm 1.04)$ to verify against the results obtained from the topoelectrical circuits (TECs), shown in Figs. 3 and 4 in the main text. For our analysis, we excite the delta-type wavefunction at the 5th node ($m = 5$). Fig. 6(a) illustrates the NHSE at the interface in the absence of any QP potential ($\lambda = 0$). The corresponding TEC analog for this scenario is depicted in Fig. 3 of the main text. Fig. 6(b) represents the system at the critical value of α , given by $\alpha_c = \ln |\max(t + \gamma, t - \gamma)/\lambda| \simeq 0.425$ for $\lambda = 1$. At this point, the eigenstates of H make a transition from exhibiting NHSE to AL, and the localization of the dynamic evolution of the wavefunction starts to shift away from the interface. For $\alpha > \alpha_c$, $|\Psi(x, t)\rangle$ no longer remains localized at the interface, as shown in Fig. 6(c). Instead, the wave propagates via quantized jumps between the AL states located at distant sites, a phenomenon termed as ‘NH jumps’⁶¹. These jumps are distinctive outcomes of the NH disorder, incorporated in our case by α . The jumps can be determined and predicted by the initial magnitude of a_k , calculated using Eq. (8), and the decay and amplification rate of each of the ψ_k , which again depends on the corresponding eigenvalues (through an exponential factor). As depicted in Fig. 6(c), the wave propagation involves several NH jumps over the observed timeframe.

APPENDIX B: LAPLACIAN OF THE TOPOELECTRICAL CIRCUIT

The TEC corresponding to the Hamiltonian, H (Eq. (7)), is constructed and analyzed in the main text. For an electrical network with $2N + 1$ nodes, which is 21 for this case ($N = 10$), let \mathcal{L} represent the Laplacian, and V_i and I_i , respectively, denote the voltage and the total current from an external source at the node i . According to Kirchhoff’s law, the following relation holds,

$$I_i = \sum_{k(i \neq k)} X_{ik} (V_i - V_k) + X_i V_i \quad \text{for } k = 1, 2, 3, \dots, 2N + 1, \quad (12)$$

where the parameters have been elaborated upon in the main text. To establish the foundation, let us now derive the Laplacian of the circuit (refer to Fig. 2(b) in the main text) under the condition where the master switch for S is open and S_1 is closed, representing the non-reciprocal circuit without the quasi-periodic (QP) potential. Following Eq. (12) without any external source

and the following $2N + 1$ equations,

$$\begin{aligned}
\frac{1}{j\omega L_{\text{edge}}} V_1 + j\omega(C - C')(V_1 - V_2) &= 0, \\
\frac{1}{j\omega L} V_2 + j\omega(C + C')(V_2 - V_1) + j\omega(C - C')(V_2 - V_3) &= 0, \\
&\vdots \\
\frac{1}{j\omega L'} V_{N+1} + j\omega(C + C')(V_{N+1} - V_N) + j\omega(C - C')(V_{N+1} - V_{N+2}) &= 0, \\
&\vdots \\
\frac{1}{j\omega L} V_{2N} + j\omega(C - C')(V_{2N} - V_{2N-1}) + j\omega(C + C')(V_{2N} - V_{2N+1}) &= 0, \\
\frac{1}{j\omega L_{\text{edge}}} V_L + j\omega(C - C')(V_{2N+1} - V_{2N}) &= 0,
\end{aligned}$$

where V_i is the voltage at i^{th} node, and the values of the circuit elements, C, C', L, L' and L_{edge} are defined in the main text. Note that j represents the imaginary number ($= \sqrt{-1}$) and $(N + 1)^{\text{th}}$ node denotes the interface. When we formulate these $2N + 1$ ($= 21$) equations corresponding to Kirchhoff's law in the form $I = \mathcal{L}V$, the resulting Laplacian matrix, \mathcal{L} is given as,

$$\mathcal{L}(\omega) = \begin{pmatrix} \frac{1}{j\omega L_{\text{edge}}} + j\omega(C - C') & -j\omega(C - C') & 0 & \cdots & \cdots \\ -j\omega(C + C') & \frac{1}{j\omega L} + 2j\omega C & -j\omega(C - C') & 0 & \cdots \\ \vdots & \vdots & \vdots & \vdots & \vdots \\ \cdots 0 & -j\omega(C + C') & \frac{1}{j\omega L'} + 2j\omega(C + C') & -j\omega(C + C') & 0 \cdots \\ \vdots & \vdots & \vdots & \vdots & \vdots \\ \cdots & 0 & -j\omega(C - C') & \frac{1}{j\omega L} + 2j\omega C & -j\omega(C + C') \\ & \cdots & 0 & -j\omega(C - C') & \frac{1}{j\omega L_{\text{edge}}} + j\omega(C - C') \end{pmatrix}$$

Note that the diagonal terms vanish at the resonant frequency,

$$\omega_R = \frac{1}{\sqrt{2LC}} = \frac{1}{\sqrt{L_{\text{edge}}(C - C')}} = \frac{1}{\sqrt{2L'(C + C')}}.$$

Subsequently, at $\omega = \omega_R$, \mathcal{L} becomes,

$$\mathcal{L}(\omega_R) = -j \begin{pmatrix} 0 & \omega_R(C - C') & 0 & \cdots & \cdots \\ \omega_R(C + C') & 0 & \omega_R(C - C') & 0 & \cdots \\ \vdots & \vdots & \vdots & \vdots & \vdots \\ \cdots 0 & \omega_R(C + C') & 0 & \omega_R(C + C') & 0 \cdots \\ \vdots & \vdots & \vdots & \vdots & \vdots \\ \cdots & 0 & \omega_R(C - C') & 0 & \omega_R(C + C') \\ & \cdots & 0 & \omega_R(C - C') & 0 \end{pmatrix} \quad (13)$$

Thus, the Laplacian, \mathcal{L} , effectively replicates the matrix form of H with $\lambda = 0$, including a scaling factor of $-j$. Consequently, the eigenvalues and the eigenvectors of \mathcal{L} directly correspond to those of H with $\lambda = 0$. This equivalence ensures that the localization properties of the eigenvectors of the TB model are reflected in the voltage profile (VP) derived from the Laplacian. Note that the capacitors are analogous to the hopping terms in the TB model, where $(t \pm \gamma) \equiv \omega_R(C \pm C')$.

Now, let us incorporate the QP potential, as described in Eq. (7), into the TEC. This addition introduces extra diagonal terms in \mathcal{L} , stemming from the node-specific values of the capacitors, $C[k]$, and the resistors, $R[k]$ at k^{th} node. According to Eq. (7), the QP potential is expressed as,

$$\lambda_k = 2\lambda \cos(2\pi\beta k + i\alpha) = 2\lambda [\cos(2\pi\beta k) \cosh \alpha - i \sin(2\pi\beta k) \sinh \alpha].$$

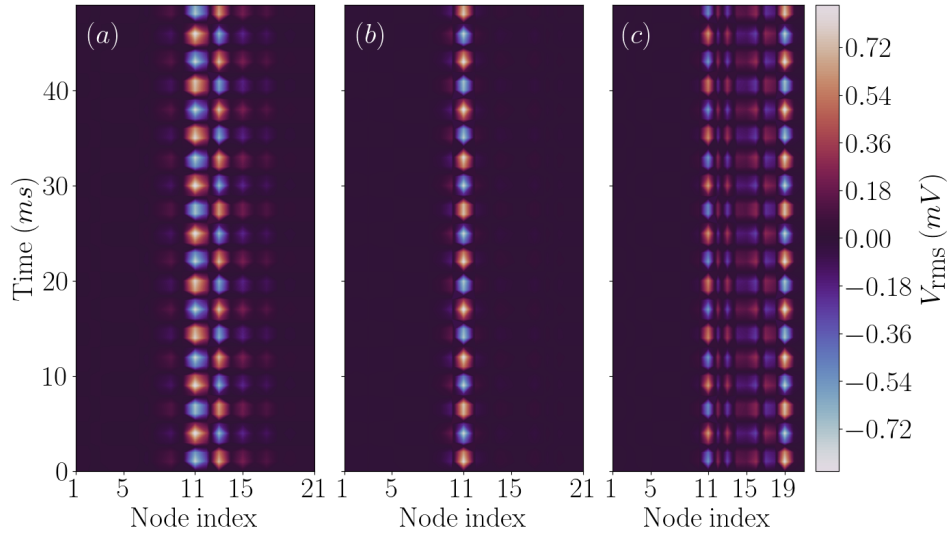


FIG. 7. The parameters λ and α for each subplot in Fig. 7 correspond directly to those in the respective subplots of Fig. 6. (a) The NHSE is evident as the $V(t)$ localizes at the interface, specifically at node 11. (b) When $\alpha = \alpha_c$, all the eigenstates of the Laplacian \mathcal{L} transform from skin states to the AL states, yet the VP remains localized at the interface. (c) Finally, for a larger value of α , the localization shifts towards the excitation node, which is the 18th node.

Thus, at the resonant frequency, ω_R , $C[k]$ and $R[k]$ take the following forms,

$$\begin{aligned} C[k] &= -\text{Re}(\lambda_k)/\omega_R = -2\lambda \cos(2\pi\beta k) \cosh \alpha / \omega_R, \\ R[k] &= [\text{Im}(\lambda_k)]^{-1} = [-2\lambda \sin(2\pi\beta k) \sinh \alpha]^{-1}. \end{aligned}$$

After including these grounded capacitors and the resistors in Eq. (13), \mathcal{L} assumes,

$$\mathcal{L} = -j \begin{pmatrix} -\omega_R C[1] + \frac{j}{R[1]} & \omega_R(C - C') & 0 & \dots & \dots \\ \omega_R(C + C') & -\omega_R C[2] + \frac{j}{R[2]} & \omega_R(C - C') & 0 & \dots \\ \vdots & \vdots & \vdots & \vdots & \vdots \\ \dots 0 & \omega_R(C + C') & -\omega_R C[N+1] + \frac{j}{R[N+1]} & \omega_R(C + C') & 0 \dots \\ \vdots & \vdots & \vdots & \vdots & \vdots \\ \dots & 0 & \omega_R(C - C') & -\omega_R C[2N] + \frac{j}{R[2N]} & \omega_R(C + C') \\ \dots & \dots & 0 & \omega_R(C - C') & -\omega_R C[2N+1] + \frac{j}{R[2N+1]} \end{pmatrix}. \quad (14)$$

Thus, Eqs. (13) and (14) represent the Laplacians for non-reciprocal TECs in absence and presence of the complex QP disorder, respectively.

APPENDIX C: COMPUTATIONAL RESULTS ON THE DYNAMICS OF THE TOPOELECTRICAL CIRCUIT

Earlier in the text, we have highlighted the difficulty of visualizing a specific eigenstate of the Laplacian, \mathcal{L} , as a measurable VP. This challenge arises because every node in the TEC network must be excited via a precisely calibrated current source. For example, to measure the k^{th} eigenstate of \mathcal{L} , denoted as V_k , the amplitude of the current source at each node must satisfy the equation,

$$I = \mathcal{L}V_k = \zeta_k V_k,$$

where ζ_k is the k^{th} eigenvalue of \mathcal{L} . To overcome this challenge, a current source, $I(t)$, can be applied at any node, and the VP ($V(t)$) can be measured at a later time. Similar to Eq. (8), $V(t)$ can also be expanded as a linear combination of the eigenvectors

of \mathcal{L} , but now, with time-dependent coefficients $a_k(t)$,

$$V(t) = \sum_{k=1} a_k(t) V_k. \quad (15)$$

Substituting these into Kirchhoff's law leads to,

$$\begin{aligned} I(t) &= \mathcal{L}V(t) = \sum_{k=1} a_k(t) \zeta_k V_k, \\ \Rightarrow a_k(t) &= \frac{V_k^\dagger I(t)}{\zeta_k}. \end{aligned} \quad (16)$$

Thus, the coefficients $a_k(t)$ can be determined at any time t once $I(t)$ is uniquely specified. We assume that V_k forms a complete orthonormal basis for \mathcal{L} with $V_a^\dagger V_b = \delta_{ab}$. Note that the values of $a_k(t=0)$ depend on the initial node of excitation.

To study the dynamical behavior of the TEC, we resort to a specific case and excite the 18th node with a current source, $I(t) = \sin(\omega_R t)$, having an amplitude of 1 mA and ω_R representing the resonant frequency of the circuit. By employing Eqs. (15) and (16), we obtain $V(t)$, which is then represented as a colormap in Fig. 7. This figure serves as the circuit analog of Fig. 6. However, unlike the TB model depicted in Fig. 6(c), no NH jumps are observed in the TEC, as shown in Fig. 7(c). Instead, the VP settles at the 19th node, located near the excitation (18th) node.

REFERENCES

- ¹P. W. Anderson, "Absence of diffusion in certain random lattices," *Phys. Rev.* **109**, 1492–1505 (1958).
- ²S. Aubry and G. André, "Analyticity breaking and anderson localization in incommensurate lattices," *Ann. Isr. Phys. Soc.* **3** (1980).
- ³S. Ganeshan, K. Sun, and S. Das Sarma, "Topological zero-energy modes in gapless commensurate aubry-andré-harper models," *Phys. Rev. Lett.* **110**, 180403 (2013).
- ⁴S. Ganeshan, J. H. Pixley, and S. Das Sarma, "Nearest neighbor tight binding models with an exact mobility edge in one dimension," *Phys. Rev. Lett.* **114**, 146601 (2015).
- ⁵G. De Tomasi, S. Bera, J. H. Bardarson, and F. Pollmann, "Quantum mutual information as a probe for many-body localization," *Phys. Rev. Lett.* **118**, 016804 (2017).
- ⁶Y. Lahini, R. Pugatch, F. Pozzi, M. Sorel, R. Morandotti, N. Davidson, and Y. Silberberg, "Observation of a localization transition in quasiperiodic photonic lattices," *Phys. Rev. Lett.* **103**, 013901 (2009).
- ⁷Y. E. Kraus, Y. Lahini, Z. Ringel, M. Verbin, and O. Zeitlinger, "Topological states and adiabatic pumping in quasicrystals," *Phys. Rev. Lett.* **109**, 106402 (2012).
- ⁸S. Dey, N. R. Das, and S. Ghosh, "Exploring unconventional features of light dynamics in aubry-andré-harper model based quasi-periodic optical lattices," *Optics Communications* **506**, 127593 (2022).
- ⁹G. Roati, C. D'Errico, L. Fallani, M. Fattori, C. Fort, M. Zaccanti, G. Modugno, M. Modugno, and M. Inguscio, "Anderson localization of a non-interacting bose-einstein condensate," *Nature* **453**, 895–898 (2008).
- ¹⁰F. A. An, K. Padavić, E. J. Meier, S. Hegde, S. Ganeshan, J. H. Pixley, S. Vishveshwara, and B. Gadway, "Interactions and mobility edges: Observing the generalized aubry-andré model," *Phys. Rev. Lett.* **126**, 040603 (2021).
- ¹¹H. Li, Y.-Y. Wang, Y.-H. Shi, K. Huang, X. Song, G.-H. Liang, Z.-Y. Mei, B. Zhou, H. Zhang, J.-C. Zhang, S. Chen, S. P. Zhao, Y. Tian, Z.-Y. Yang, Z. Xiang, K. Xu, D. Zheng, and H. Fan, "Observation of critical phase transition in a generalized aubry-andré-harper model with superconducting circuits," *npj Quantum Information* **9**, 40 (2023).
- ¹²T. E. Lee, "Anomalous edge state in a non-hermitian lattice," *Phys. Rev. Lett.* **116**, 133903 (2016).
- ¹³H. Shen, B. Zhen, and L. Fu, "Topological band theory for non-hermitian hamiltonians," *Phys. Rev. Lett.* **120**, 146402 (2018).
- ¹⁴Y. Ashida, Z. Gong, and M. Ueda, "Non-hermitian physics," *Advances in Physics* **69**, 249–435 (2020).
- ¹⁵E. J. Bergholtz, J. C. Budich, and F. K. Kunst, "Exceptional topology of non-hermitian systems," *Rev. Mod. Phys.* **93**, 015005 (2021).
- ¹⁶S. Yao and Z. Wang, "Edge states and topological invariants of non-hermitian systems," *Phys. Rev. Lett.* **121**, 086803 (2018).
- ¹⁷C. H. Lee and R. Thomale, "Anatomy of skin modes and topology in non-hermitian systems," *Phys. Rev. B* **99**, 201103 (2019).
- ¹⁸N. Okuma, K. Kawabata, K. Shiozaki, and M. Sato, "Topological origin of non-hermitian skin effects," *Phys. Rev. Lett.* **124**, 086801 (2020).
- ¹⁹M.-H. L. Xiujuan Zhang, Tian Zhang and Y.-F. Chen, "A review on non-hermitian skin effect," *Advances in Physics: X* **7**, 2109431 (2022).
- ²⁰W. D. Heiss, "The physics of exceptional points," *Journal of Physics A: Mathematical and Theoretical* **45**, 444016 (2012).
- ²¹D. Leykam, K. Y. Bliokh, C. Huang, Y. D. Chong, and F. Nori, "Edge modes, degeneracies, and topological numbers in non-hermitian systems," *Phys. Rev. Lett.* **118**, 040401 (2017).
- ²²K. Yokomizo and S. Murakami, "Non-bloch band theory of non-hermitian systems," *Phys. Rev. Lett.* **123**, 066404 (2019).
- ²³T. Eichelkraut, R. Heilmann, S. Weimann, S. Stützer, F. Dreisow, D. N. Christodoulides, S. Nolte, and A. Szameit, "Mobility transition from ballistic to diffusive transport in non-hermitian lattices," *Nature Communications* **4**, 2533 (2013).
- ²⁴R. El-Ganainy, K. G. Makris, M. Khajavikhan, Z. H. Musslimani, S. Rotter, and D. N. Christodoulides, "Non-hermitian physics and pt symmetry," *Nature Physics* **14**, 11–19 (2018).
- ²⁵A. Wang, Z. Meng, and C. Q. Chen, "Non-hermitian topology in static mechanical metamaterials," *Science Advances* **9** (2023), 10.1126/sciadv.adf7299.
- ²⁶R. Fleury, D. Sounas, and A. Alù, "An invisible acoustic sensor based on parity-time symmetry," *Nat. Commun.* **6** (2015), 10.1038/ncomms6905.
- ²⁷T. Guo, B. Assouar, B. Vincent, and A. Merkel, "Edge states in non-hermitian composite acoustic schrödinger heeger chains," *Journal of Applied Physics* **135**, 043102 (2024).
- ²⁸M. Peng, C. Wu, Z. Cui, X. Zhang, Q. Wei, M. Yan, and G. Chen, "Acoustic non-hermitian dirac states tuned by flexible designed gain and loss," *Applied Physics Letters* **125**, 193101 (2024).
- ²⁹N. Hatano and D. R. Nelson, "Localization transitions in non-hermitian quantum mechanics," *Phys. Rev. Lett.* **77**, 570–573 (1996).
- ³⁰S. Longhi, "Topological phase transition in non-hermitian quasicrystals," *Phys. Rev. Lett.* **122**, 237601 (2019).
- ³¹S. Schiffer, X.-J. Liu, H. Hu, and J. Wang, "Anderson localization transition in a robust $\mathcal{P}\mathcal{T}$ -symmetric phase of a generalized aubry-andré model," *Phys. Rev. A* **103**, L011302 (2021).
- ³²S. Longhi, "Phase transitions in a non-hermitian aubry-andré-harper model," *Phys. Rev. B* **103**, 054203 (2021).
- ³³Y. Liu, Q. Zhou, and S. Chen, "Localization transition, spectrum structure, and winding numbers for one-dimensional non-hermitian quasicrystals," *Phys. Rev. B* **104**, 024201 (2021).

- ³⁴X. Cai, “Localization transitions and winding numbers for non-hermitian aubry-andré-harper models with off-diagonal modulations,” *Phys. Rev. B* **106**, 214207 (2022).
- ³⁵S. Gandhi and J. N. Bandyopadhyay, “Topological triple phase transition in non-hermitian quasicrystals with complex asymmetric hopping,” *Phys. Rev. B* **108**, 014204 (2023).
- ³⁶Y.-M. Sun, X.-Y. Wang, and L.-J. Zhai, “Hybrid scaling properties of the localization transition in a non-hermitian disordered aubry-andré model,” *Phys. Rev. B* **110**, 054202 (2024).
- ³⁷S.-Z. Li, E. Cheng, S.-L. Zhu, and Z. Li, “Asymmetric transfer matrix analysis of lyapunov exponents in one-dimensional nonreciprocal quasicrystals,” *Phys. Rev. B* **110**, 134203 (2024).
- ³⁸V. V. Albert, L. I. Glazman, and L. Jiang, “Topological properties of linear circuit lattices,” *Phys. Rev. Lett.* **114**, 173902 (2015).
- ³⁹C. H. Lee, S. Imhof, C. Berger, F. Bayer, J. Brehm, L. W. Molenkamp, T. Kiessling, and R. Thomale, “Topoelectrical circuits,” *Communications Physics* **1**, 39 (2018).
- ⁴⁰T. Helbig, T. Hofmann, C. H. Lee, R. Thomale, S. Imhof, L. W. Molenkamp, and T. Kiessling, “Band structure engineering and reconstruction in electric circuit networks,” *Phys. Rev. B* **99**, 161114 (2019).
- ⁴¹J. Dong, V. Juričić, and B. Roy, “Topoelectric circuits: Theory and construction,” *Phys. Rev. Res.* **3**, 023056 (2021).
- ⁴²S. Guo, G. Pan, J. Huang, R. Huang, F. Zhuang, S. Su, Z. Lin, W. Qiu, and Q. Kan, “Realization of the square-root higher-order topology in decorated su–schrieffer–heeger electric circuits,” *Applied Physics Letters* **123**, 043102 (2023).
- ⁴³H. Yang, L. Song, Y. Cao, and P. Yan, “Circuit realization of topological physics,” *Physics Reports* **1093**, 1–54 (2024), circuit realization of topological physics.
- ⁴⁴T. Helbig, T. Hofmann, S. Imhof, M. Abdelghany, T. Kiessling, L. W. Molenkamp, C. H. Lee, A. Szameit, M. Greiter, and R. Thomale, “Generalized bulk–boundary correspondence in non-hermitian topoelectrical circuits,” *Nature Physics* **16**, 747–750 (2020).
- ⁴⁵B. Liu, Y. Li, B. Yang, X. Shen, Y. Yang, Z. H. Hang, and M. Ezawa, “Experimental observation of non-hermitian higher-order skin interface states in topological electric circuits,” *Phys. Rev. Res.* **5**, 043034 (2023).
- ⁴⁶W. Lin, B. Ruan, C. Liu, X. Dai, and Y. Xiang, “Evolution of topological extended state in multidimensional non-hermitian topoelectrical circuits,” *Applied Physics Letters* **125**, 173104 (2024).
- ⁴⁷D. Halder, R. Thomale, and S. Basu, “Circuit realization of a two-orbital non-hermitian tight-binding chain,” *Phys. Rev. B* **109**, 115407 (2024).
- ⁴⁸C.-X. Guo, L. Su, Y. Wang, L. Li, J. Wang, X. Ruan, Y. Du, D. Zheng, S. Chen, and H. Hu, “Scale-tailored localization and its observation in non-hermitian electrical circuits,” *Nature Communications* **15**, 9120 (2024).
- ⁴⁹S. M. Rafi-Ul-Islam, Z. B. Siu, M. S. H. Razo, and M. B. A. Jalil, “Dynamic manipulation of non-hermitian skin effect through frequency in topoelectrical circuits,” (2024), arXiv:2410.16914 [cond-mat.mes-hall].
- ⁵⁰H. Jiang, L.-J. Lang, C. Yang, S.-L. Zhu, and S. Chen, “Interplay of non-hermitian skin effects and anderson localization in nonreciprocal quasiperiodic lattices,” *Phys. Rev. B* **100**, 054301 (2019).
- ⁵¹Q.-B. Zeng and Y. Xu, “Winding numbers and generalized mobility edges in non-hermitian systems,” *Phys. Rev. Res.* **2**, 033052 (2020).
- ⁵²X. Xia, K. Huang, S. Wang, and X. Li, “Exact mobility edges in the non-hermitian t_1-t_2 model: Theory and possible experimental realizations,” *Phys. Rev. B* **105**, 014207 (2022).
- ⁵³S. Ganguly and S. K. Maiti, “Electrical analogue of one-dimensional and quasi-one-dimensional aubry–andré–harper lattices,” *Scientific Reports* **13**, 13633 (2023).
- ⁵⁴H. Wang, W. Zhang, H. Sun, and X. Zhang, “Observation of non-abelian anderson localization and transition in topoelectrical circuits,” *Phys. Rev. B* **108**, 144203 (2023).
- ⁵⁵F. Y. Wu, “Theory of resistor networks: the two-point resistance,” *Journal of Physics A: Mathematical and General* **37**, 6653 (2004).
- ⁵⁶A. Avila, “Global theory of one-frequency Schrödinger operators,” *Acta Mathematica* **215**, 1–54 (2015).
- ⁵⁷S. Weidemann, M. Kremer, T. Helbig, T. Hofmann, A. Stegmaier, M. Greiter, R. Thomale, and A. Szameit, “Topological funneling of light,” *Science* **368**, 311–314 (2020).
- ⁵⁸S. Weidemann, M. Kremer, S. Longhi, and A. Szameit, “Coexistence of dynamical delocalization and spectral localization through stochastic dissipation,” *Nature Photonics* **15**, 576–581 (2021).
- ⁵⁹A. F. Tzortzakakis, K. G. Makris, A. Szameit, and E. N. Economou, “Transport and spectral features in non-hermitian open systems,” *Phys. Rev. Res.* **3**, 013208 (2021).
- ⁶⁰A. Chakrabarty and S. Datta, “Skin effect and dynamical delocalization in non-hermitian quasicrystals with spin-orbit interaction,” *Phys. Rev. B* **107**, 064305 (2023).
- ⁶¹A. Leventis, K. G. Makris, and E. N. Economou, “Non-hermitian jumps in disordered lattices,” *Phys. Rev. B* **106**, 064205 (2022).